NASA/CR-2019-220335

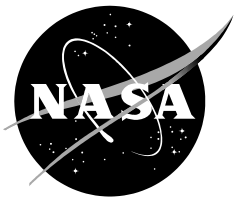

Post-test Microstructural Analysis of Particle Impact-Tested Wrought Inconel, Additively Manufactured Inconel and Wrought Monel Targets

Ngozi C. Ochoa[1]
Jonathan M. Tylka

[1]*Materials Engineer Co-op, Jacobs Technology Test2 Contract*
NASA Johnson Space Center White Sands Test Facility
P.O. Box 20, Las Cruces, NM 880042

National Aeronautics and Space Administration

Johnson Space Center Houston,
Texas 77058

August 2019

NASA STI Program Office ... in Profile

Since its founding, NASA has been dedicated to the advancement of aeronautics and space science. The NASA scientific and technical information (STI) program plays a key part in helping NASA maintain this important role.

The NASA STI program operates under the auspices of the Agency Chief Information Officer. It collects, organizes, provides for archiving, and disseminates NASA's STI. The NASA STI program provides access to the NTRS Registered and its public interface, the NASA Technical Report Server, thus providing one of the largest collections of aeronautical and space science STI in the world. Results are published in both non-NASA channels and by NASA in the NASA STI Report Series, which includes the following report types:

- TECHNICAL PUBLICATION. Reports of completed research or a major significant phase of research that present the results of NASA Programs and include extensive data or theoretical analysis. Includes compilations of significant scientific and technical data and information deemed to be of continuing reference value. NASA counter-part of peer-reviewed formal professional papers but has less stringent limitations on manuscript length and extent of graphic presentations.

- TECHNICAL MEMORANDUM. Scientific and technical findings that are preliminary or of specialized interest, e.g., quick release reports, working papers, and bibliographies that contain minimal annotation. Does not contain extensive analysis.

- CONTRACTOR REPORT. Scientific and technical findings by NASA-sponsored contractors and grantees.

- CONFERENCE PUBLICATION. Collected papers from scientific and technical conferences, symposia, seminars, or other meetings sponsored or co-sponsored by NASA.

- SPECIAL PUBLICATION. Scientific, technical, or historical information from NASA programs, projects, and missions, often concerned with subjects having substantial public interest.

- TECHNICAL TRANSLATION. English-language translations of foreign scientific and technical material pertinent to NASA's mission.

Specialized services also include organizing and publishing research results, distributing specialized research announcements and feeds, providing information desk and personal search support, and enabling data exchange services.

For more information about the NASA STI program, see the following:

- Access the NASA STI program home page at *http://www.sti.nasa.gov*

- E-mail your question to help@sti.nasa.gov

- Phone the NASA STI Information Desk at 757-864-9658

- Write to:
  NASA STI Information Desk
  Mail Stop 148
  NASA Langley Research Center
  Hampton, VA 23681-2199

NASA/CR-2019-220335

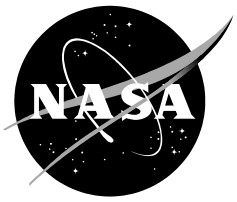

Post-test Microstructural Analysis of Particle Impact-Tested Wrought Inconel, Additively Manufactured Inconel and Wrought Monel Targets

Ngozi C. Ochoa[1]
Jonathan M. Tylka

[1]*Materials Engineer Co-op, Jacobs Technology Test2 Contract*
NASA Johnson Space Center White Sands Test Facility
P.O. Box 20, Las Cruces, NM 880042

National Aeronautics and Space Administration

Johnson Space Center Houston,
Texas 77058

August 2019

Available from:

NASA STI Program
Mail Stop 148
NASA Langley Research Center
Hampton, VA 23681-2199

National Technical Information Service
5285 Port Royal Road
Springfield, VA 22161

This report is also available in electronic form at http://www.sti.nasa.gov/ and http://ntrs.nasa.

Table of Contents

1.0 INTRODUCTION 1
2.0 EXPERIMENTAL METHODS 1
3.0 EXPERIMENTAL RESULTS 3
3.1 Surface characterization of wrought IN718 3
3.2 Surface characterization of AM-IN718 8
3.3 Surface characterization of Monel 400 11
3.4 Microstructural analysis 14
3.5 Velocity approximation 19
4.0 DISCUSSION 20
5.0 FUTURE WORK 20

(This page intentionally left blank)

1.0 INTRODUCTION

Particle impact testing in high-pressure oxygen was performed to evaluate ignition suscetibility of Inconel 718 and Monel 400. Sapphire particles (1.5-mm diameter) under high-pressure oxygen, travelling at hypersonic speeds, made impact with metal targets, resulting in surface indentations. This report details the post-test characterization of impact craters observed on three metallic target samples: wrought nickel-based superalloy Inconel 718 (IN718), additively manufactured Inconel 718 (AM-IN718) and nickel-copper alloy, Monel 400.

2.0 EXPERIMENTAL METHODS

Surface characterization was performed by light optical microscopy (LOM) and scanning electron microscopy (SEM), including use of the energy dispersive spectroscopy (EDS) capability of the SEM for chemical analysis. Impact crater penetration depth measurements were obtained utlizing the working distance of the electron beam. Penetration depth measurements were not obtained for partial craters or impact craters that contained overlapping with other impact craters. Impact crater measurements are summarized in Table 1.

Table 1 – Impact Crater Test Data

Test Target	Impact crater	Sample test surface thickness (mm)	Mass, pre-test (g)	Mass, post-test (g)	Depth (P) of impact crater (mm)	Diameter of impact crater (mm)	Test Temperature (F)
Wrought IN718	C	1.270	2.803	2.803	0.268	1.38	850
AM-IN718	A	1.544	2.882	2.882	0.293	0.449	770
Monel 400	E	1.689	2.798	2.577	0.449	1.51	834

Hardness measurements were obtained for tested and untested wrought IN718, AM IN718 and Monel 400 targets. Testing was carried out with a Rockwall superficial brale indenter for Inconel samples under an indentation load of 30-kgf (HR 30-N) and a diamond indentor under indentation loads was used for Monel Samples (HR 30-T). Hardness measurements for untested targets were obtained from the impact test surface (A), the outer diameter wall surface (B) and the bottom hollowed base surface (C). A schematic of the impact test target is provided in FIG. 1. For tested samples, hardness was only measured on surface C.

Impact craters were bisected, off-center, with a 0.006-in. wire by electrical discharge machining. The axial cross-section containing more crater volume was metallographically prepared by standard polishing techniques and mounted in epoxy thermoset resin. Stereomicroscopy was utilized for dimensional analysis and microstructural evaluation was achieved by use of LOM subsequent to chemically etching (45-mL HCl, 15-mL HNO_3, 5-mL HF, and 85-mL H_20 for IN718 samples and 10-g $CuSO_4$, 50-mL HCl, 50-mL H_20 for the Monel sample). Terminal ballistics was employed to predict impact velocity of projectile.

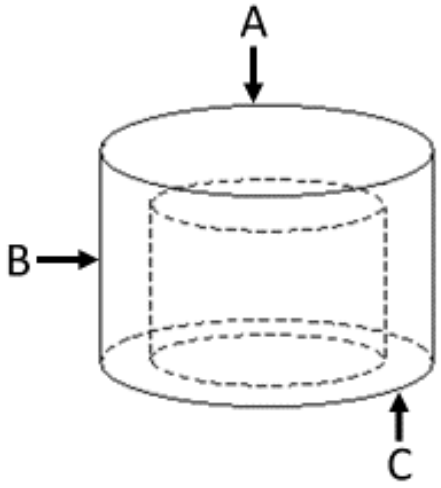

FIG. 1 – Schematic of particle impact test target. Arrows A, B and C indicate surface from which hardness testing was carried out.

3.0 EXPERIMENTAL RESULTS

3.1 Surface characterization of wrought IN718

The wrought IN718 particle impact samples contained three primary impact craters and six smaller secondary impact craters, FIG. 2. Craters A and B were shown to be the result of two separate impact events occuring in the same region, the impact at Crater A assumed to precede the impact at Crater B.

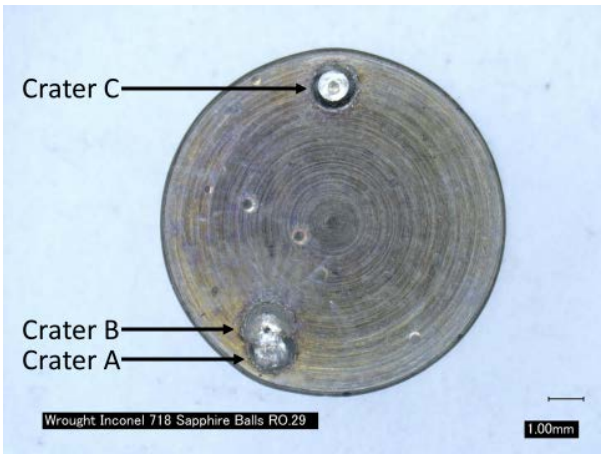

FIG. 2 – Wrought IN718 particle impact test target.

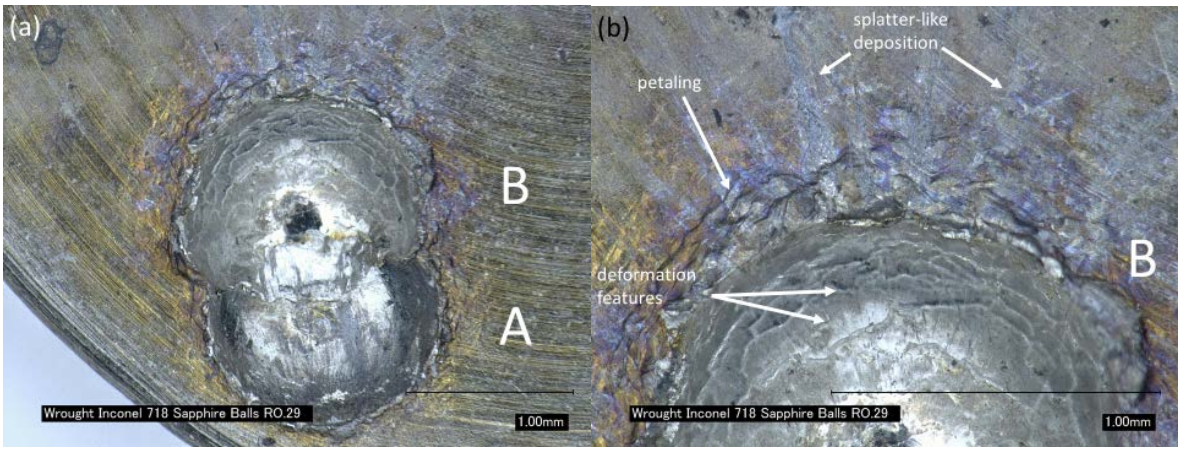

FIG. 3 – Wrought IN718 particle impact test target (a) Crater A and Crater B (b) Crater C.

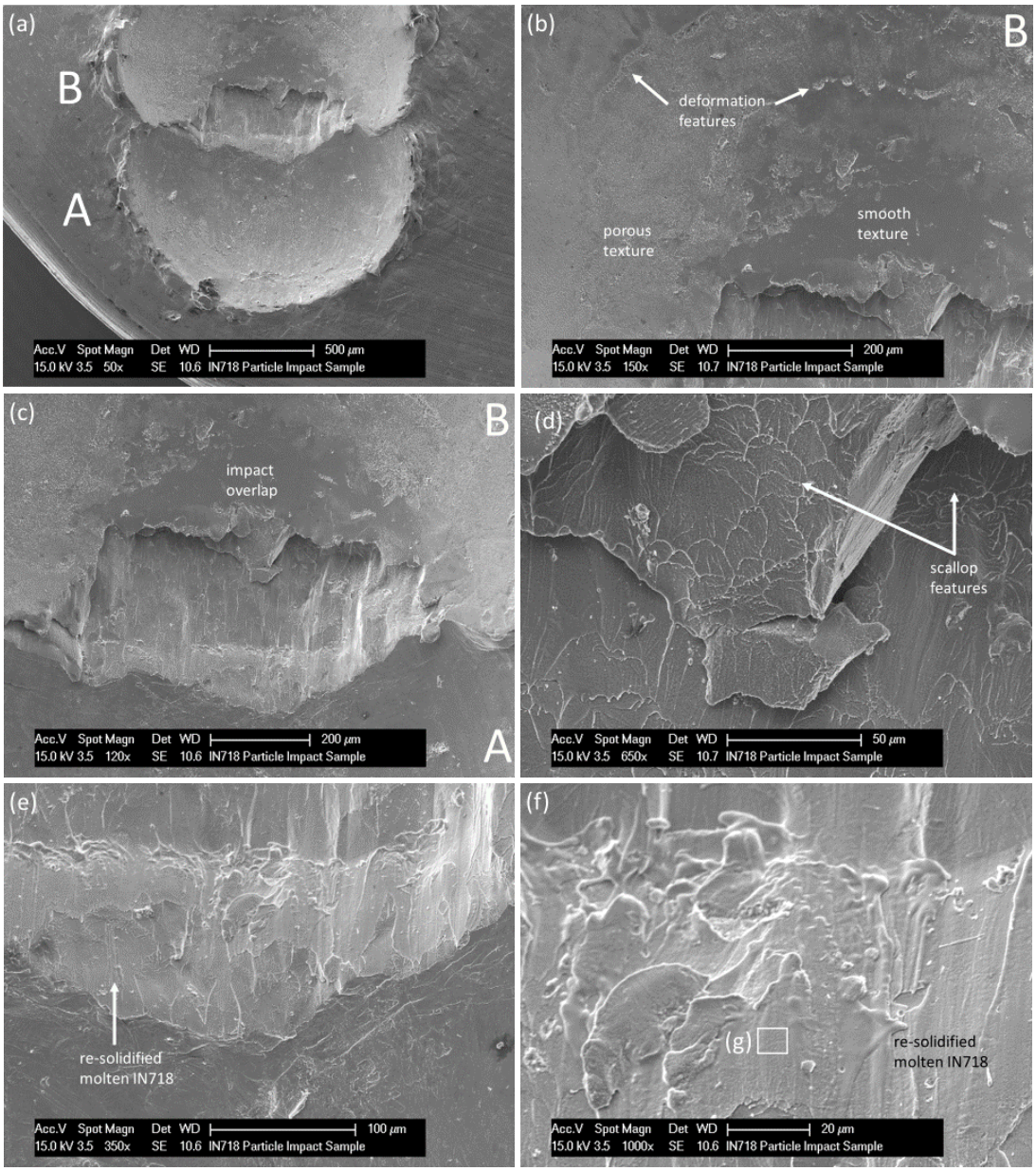

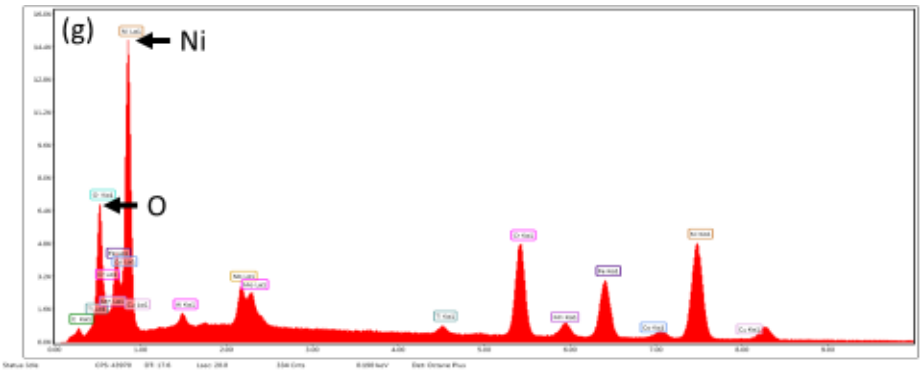

FIG. 4 – (a)-(f) Scanning electron micrographs of wrought IN718 particle impact test target, Crater A and Crater B overlap (g) EDAX spectrum of area g outlined in (f).

The undisturbed surfaces of the sample were dull in appearance compared to the bright, shiny interior surfaces of the craters. Illustrated in FIG. 3, purple-colored, powder-like deposition was observed on the undisturbed surfaces surrounding the craters, with the highest color intensity seen in the areas of Crater A and Crater B. Adjacent to Crater B, the purple features possessed a distinct splatter pattern that emanated from the crater perimeter. Deformation of the sample was observed at the surfaces adjacent to the impact craters. The deformation was observed as a perimeter of surface ridges, oriented circumferential to the impact crater, extending outward – a phenomenon termed as petaling.

The interior walls of the primary impact craters contained circumferential and radial features of deformation nearest to the crater perimeter, characterized by a rough, porous texture, FIG. 4(a-b). Moving radially inward towards the floor of the crater, the interior wall texture appeared increasingly smooth. The contrasting textures were distinct, as the porous texture was observed as a lighter color and the smooth texture observed as a darker color in electron micrographs. Evidence of melting was observed at the region of impact overlap between A and B with scallop features indicating melt flow on fracture surfaces seen within this region, FIG. 4(c-f).

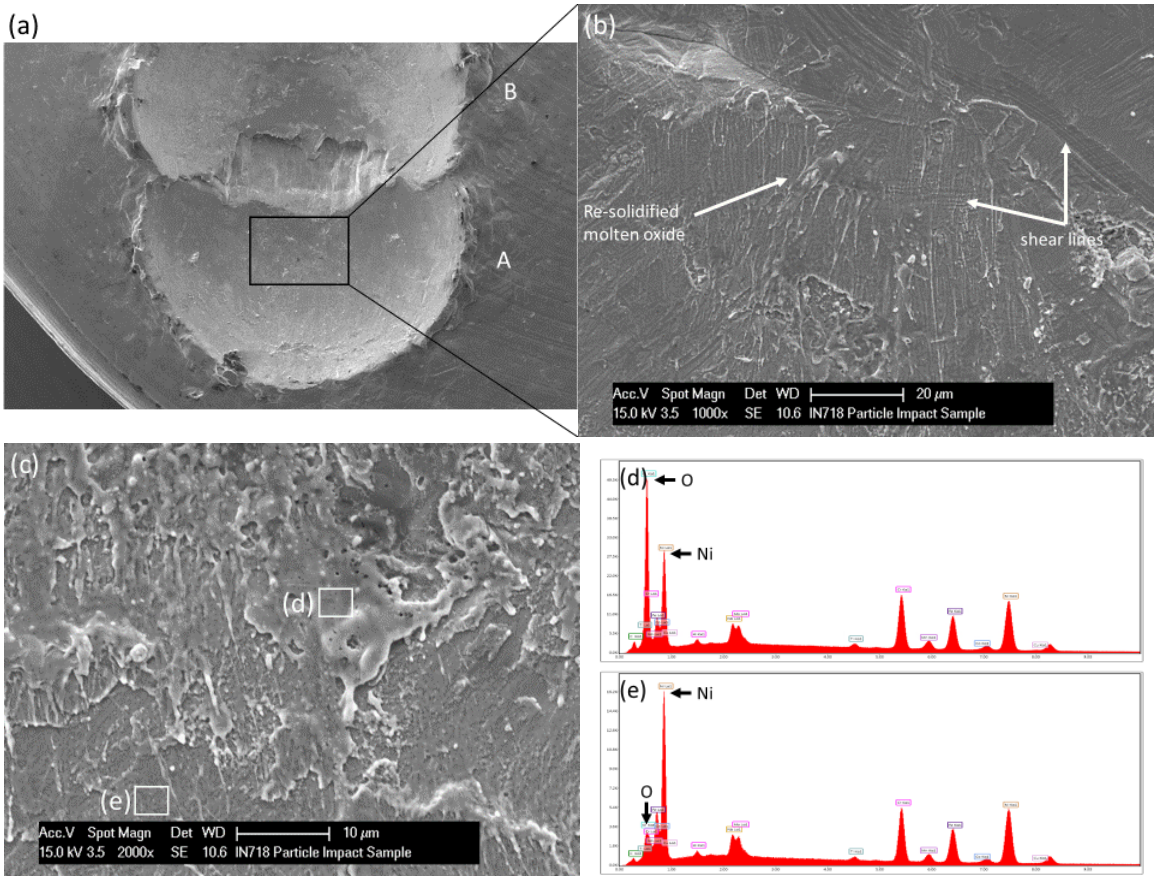

FIG. 5 – (a) Scanning electron micrographs of wrought IN718 particle impact test target, Crater A and Crater B overlap; (b)-(c) close-up view of region outlined in (a); (d)-(e) EDAX spectrum of area g outlined in (c).

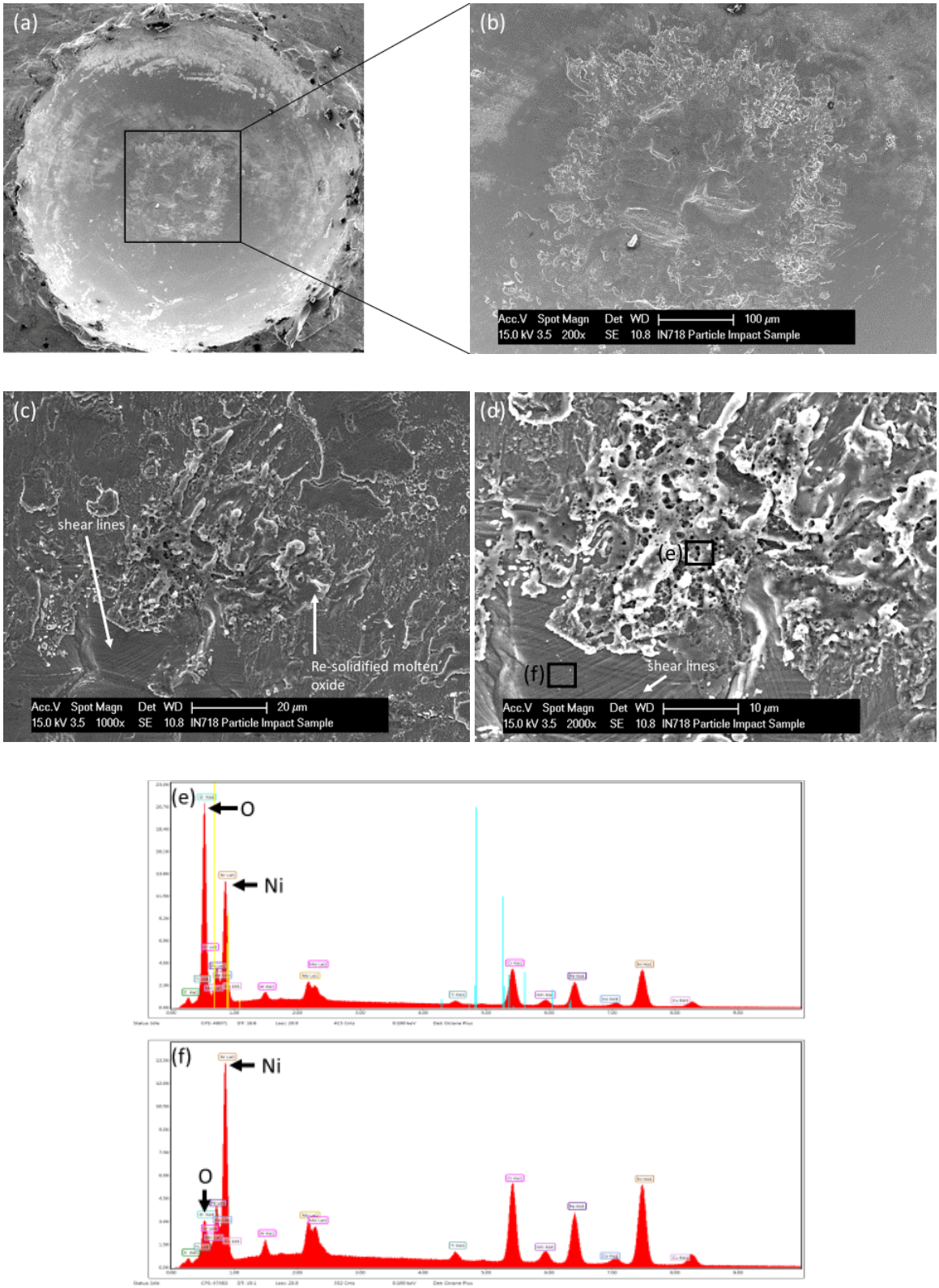

FIG. 6 – (a) Scanning electron micrographs of wrought IN718 particle impact test target, Crater C; (b)-(d) close-up view of region outlined in (a); (e)-(f) EDAX spectrum of corresponding areas outlined in (c).

As shown in FIG. 5 and FIG. 6, a circular region of resolidified molten material and multidirectional shear bands were observed at the floor of Craters A and C. The spectra obtained by EDS confirmed the resolidified molten material at the depths of Craters A and C to be oxygen-rich, while the resolidified molten material at Crater A-B impact overlap contained mostly nickel.

Regional elemental mapping provided a clear outline of the deposition splatter pattern emanating from Crater B, and results revealed the purple-colored splatter to be localized regions of increased oxygen concentration. Coarse, oxygen-rich particles were seen unevenly distrubuted along the undisturbed sample surface and within impact craters. Within Crater A, increased oxygen concetration was characterized by a ring-like shape at the crater floor and an irregular, smear-like pattern along the crater walls. Localized oxygen was shown to have a distinct ring-shape pattern at the depth of Crater C, with all other surfaces of the crater exhibiting markedly less oxygen.

The presence of increased aluminum was observed on the undisturbed test surface and appeared as concentric rings, appearing to be a result of machining. The interior surfaces of impact craters, exhibiting significantly low amounts of aluminum, contained Al-rich particles, some of which were also rich in oxygen as indicated by white arrows in FIG. 8.

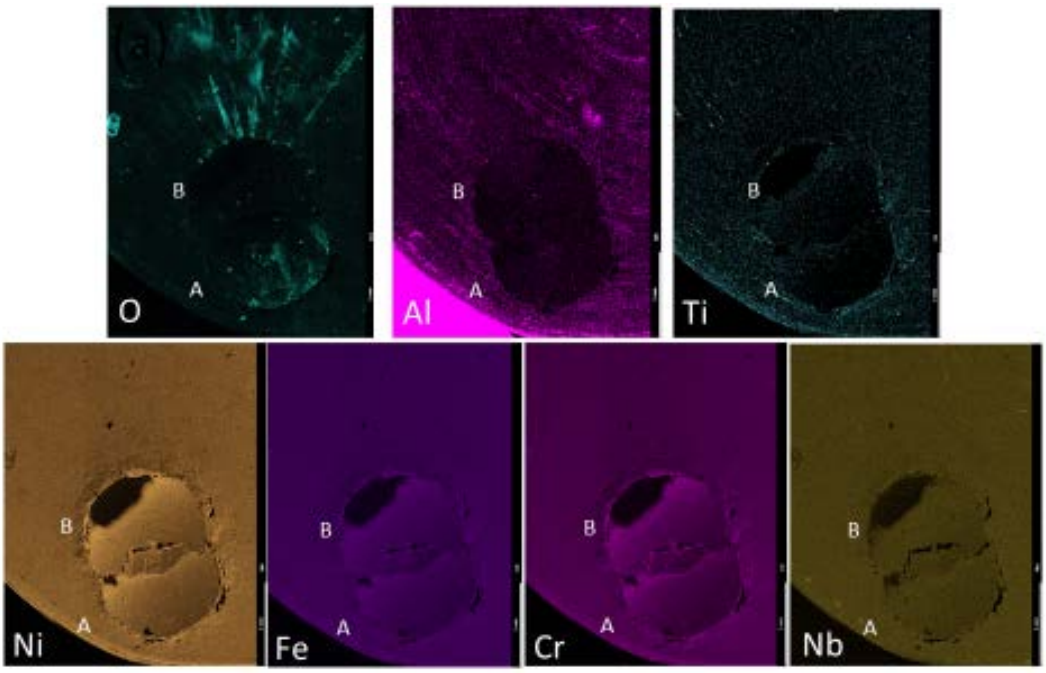

FIG. 7 – Elemental EDS maps of wrought IN718 particle impact test target, Crater A and Crater B.

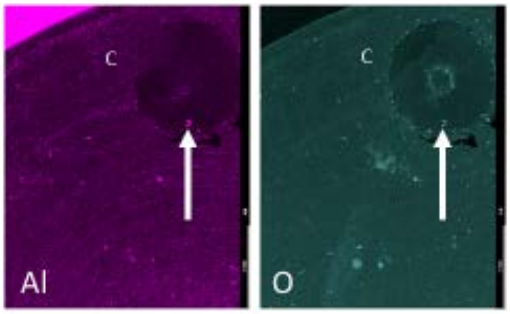

FIG. 8 – Elemental EDS maps of wrought IN718 particle impact test target, Crater C.

3.2 Surface characterization of AM-IN718

The particle impact target composed of AM-IN718 contained one primary impact crater and one smaller secondary impact crater, FIG. 9. On undisturbed surfaces of the test surface, a columnar texture resulting from the selective laser melting process was distinct. Contributing to the striped characteristic of the surface, the texture consisted of distinct, dark columns of melt pools with inter-melt pool regions appearing light and featureless, shown in FIG. 10.

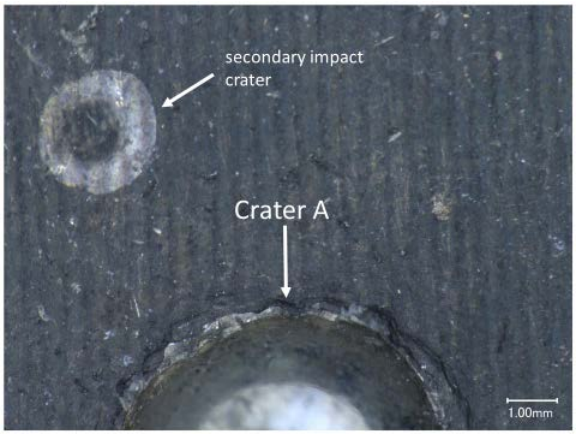

FIG. 9 – AM-IN718 particle impact test target, Crater A, and secondary impact crater.

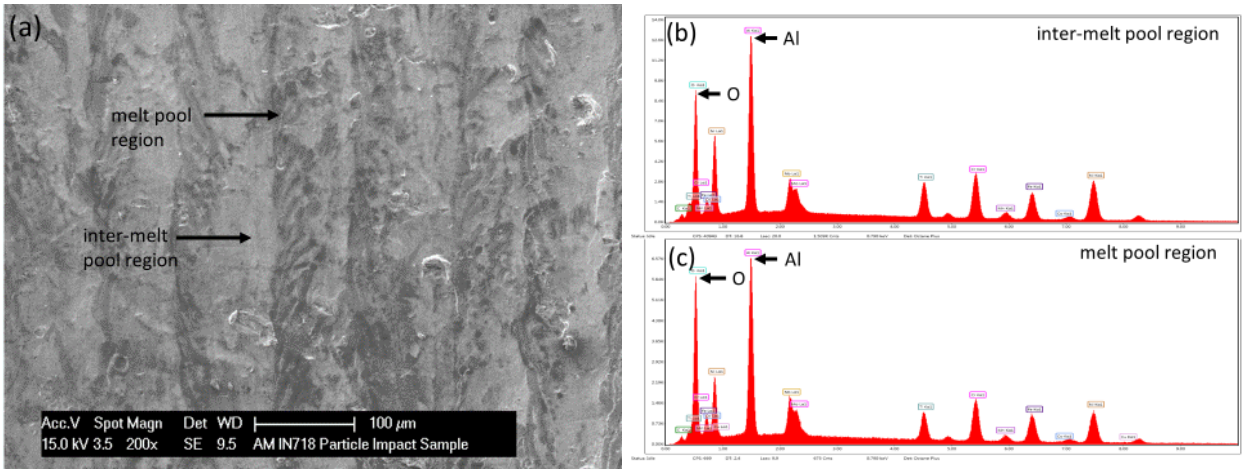

FIG. 10 – (a) Scanning electron micrograph of AM-IN718 particle impact test target, undisturbed surface with raster shown, undisturbed test surface; (b) inter-melt pool region; and (c) melt pool region.

The columnar surface texture was absent throughout the majority of the impact crater surface, maintained only at the impact crater floor in a 0.70-μm-diameter region. FIG. 11(a-b) provide an image of the crater floor where the melt pool regions appeared deformed and exhibited cracking, contrasting with the globular, script-like nature of the melt pools observed on undisturbed test surfaces presented in FIG. 10. FIG. 11(b) also provides a close-up view of shiny, angular particles that appear embedded into the crater floor. The crater floor also contained mud-cracking and rough surface texture in regions adjacent to deformed melt pool columns, FIG. 11(c).

As seen within craters of the wrought IN718 target, the interior surface of the impact crater contained circumferential and radial features of deformation; however, unlike the wrought target, the rough and porous region of deformation was not seen consistently along the walls nearest to the crater perimeter, but in a localized region as shown in FIG. 11(d). Petaling features were also seen, visible in FIG. 11(d), with variable thickness extending along the primary crater perimeter of AM-IN718.

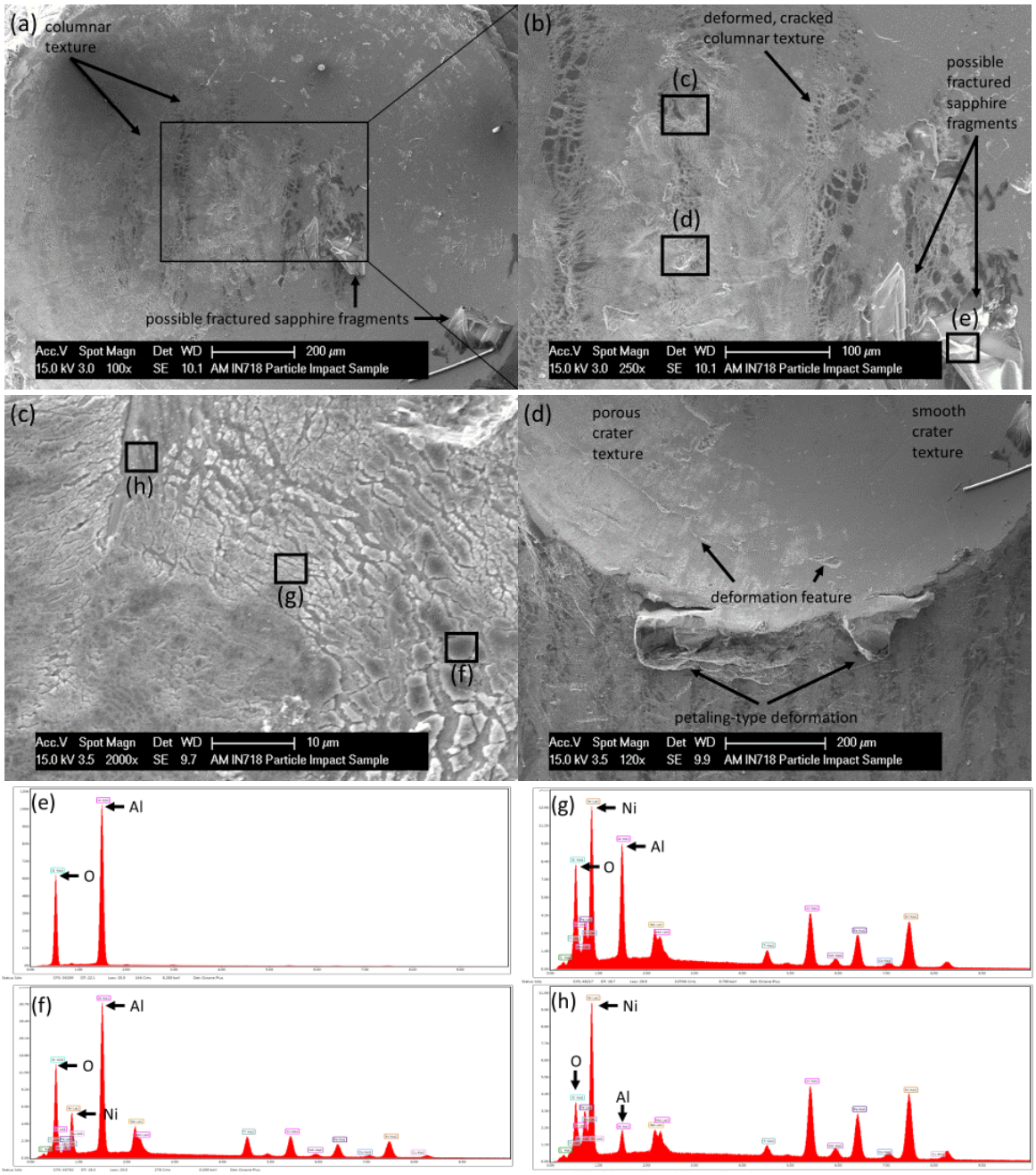

FIG. 11 – Scanning electron micrographs of AM-IN718 particle impact test target, Crater A: (a-b) crater floor; (c) close-up view of corresponding area in (b); (d) crater wall; (e-h) EDAX spectrum of corresponding region outlined in (b) and (c).

Surface oxidation of the AM718 sample was also revealed with relatively high intensity peaks corresponding to aluminum and oxygen detected and a relative increase in O detected within the melt pool region, FIG. 10. The spectrum provided in FIG. 11(e), obtained by EDS, confirmed the embedded particle to contain only Al and O, suggesting this particle to be a fractured sapphire projectile. At the crater floor, increased relative intensity for oxygen was also observed for the mud-cracked features with adjacent regions beneath mud-cracked features composed of predominately nickel.

Regional elemental mapping revealed the crater walls predominantly absent of aluminum, titanium with the exception of a distint circular region at the crater floor. Increased relative intensity for nickel, along with major alloying elements, Fe and Cr was observed within the impact crater where Al and Ti were nearly absent.

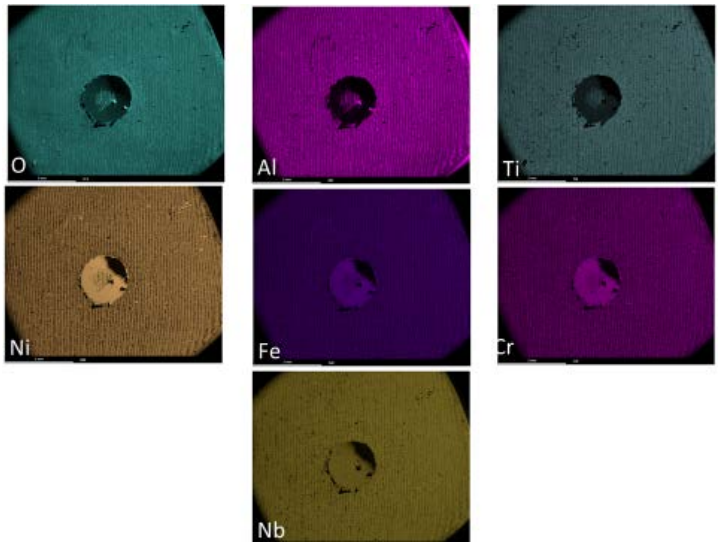

FIG. 12 – Elemental EDS maps of AM-IN718 particle impact test target, Crater A.

3.3 Surface characterization of Monel 400

The Monel particle impact sample contained nine primary impact craters and eight secondary impact craters, FIG. 13. Blue discoloration was observed on undisturbed surfaces nearest to the impact craters. The interior surfaces of the impact craters were remarkably smooth compared to those of the wrought and AM-IN718 samples. Petaling at impact craters were prounounced, as material deformation at the perimeter was characterized as smooth with variable thickness extending along the crater perimeter. Deformation seen at the rim did not extend significantly into the undisturbed sample surface, as no bulging was observed.

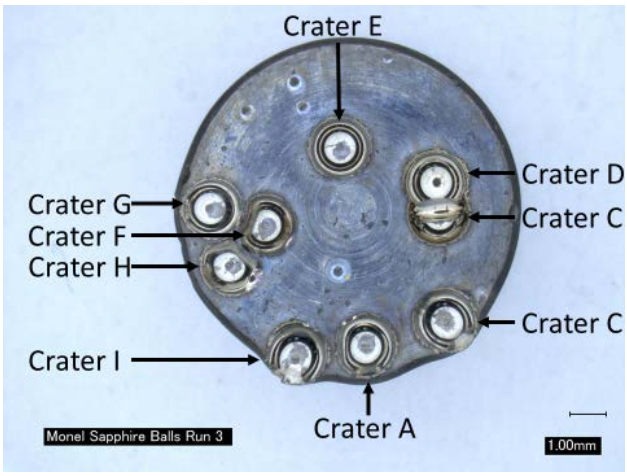

FIG. 13 – Wrought Monel 400 particle impact test target.

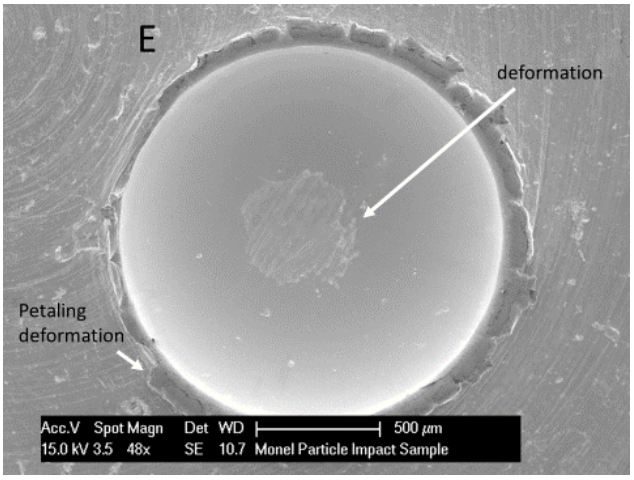

FIG. 14 – Scanning electron micrograph of Monel 400 particle impact test target, Crater E.

A circular region of deformed, resolidifed molten material was observed at the floor of all craters, FIG. 15a. Higher maginifcation, provided in FIG. 15b, revealed a smear-like texture of the deformation and chemical analysis identified this region to contain primarily nickel. Regions of the crater wall, nearest to the perimeter, were characterized by a streak-like formation. The white regions were porous in texture while adjacent, darker regions contained the same smooth texture observed throughout the majority of the crater walls.

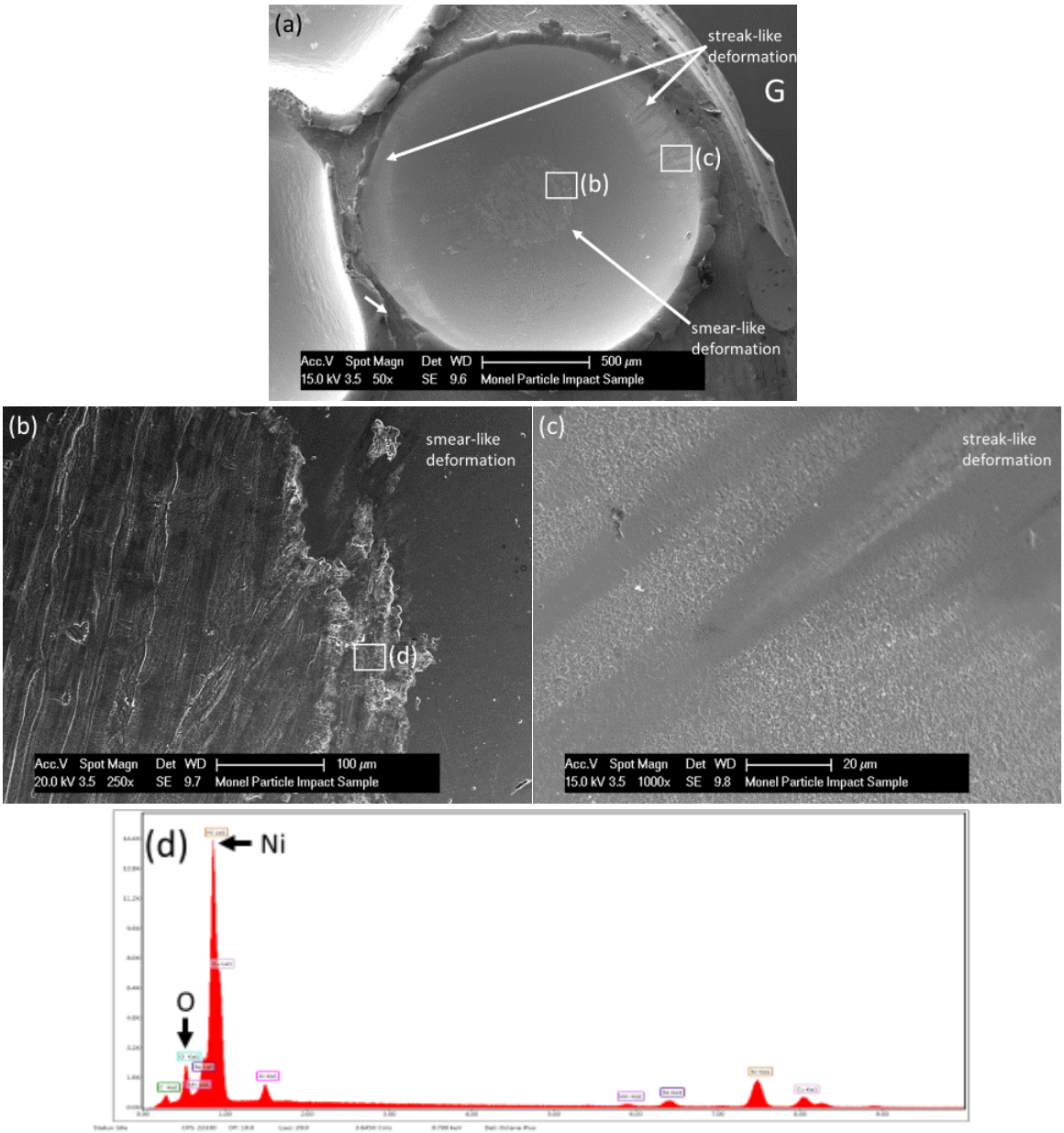

FIG. 15 – (a) Scanning electron micrographs of Monel 400 particle impact test target, Crater G; (b)-(c) close-up of corresponding regions outlined in (a); (d) EDAX spectrum of region outlined in (b).

From EDS mapping results of Craters F, G and H on the Monel 400 test target, surface oxidation is revealed, along with localized oxygen-rich regions throughout the undisturbed test surface and along crater surfaces. An oxygen-rich circular region, similar to those seen within craters of IN718 targets, was apparent at crater floors, with oxygen also exhibiting a splatter-like arrangement on the wall surfaces of Crater G. This splatter-like feature was also seen at the intersection of crater overlap as well as on undisturbed surfaces adjacent to Crater G.

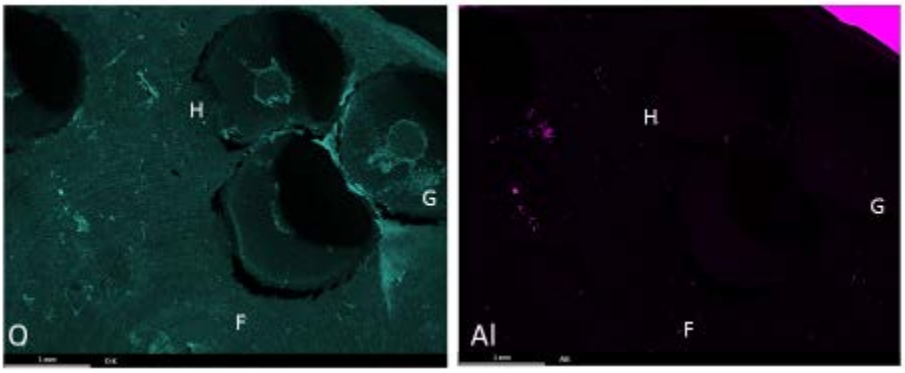

FIG. 16 – Elemental EDS maps of Monel 400 particle impact test target, Crater F, G and H.

3.4 Microstructural analysis

The untested wrought IN718 microstructure consisted of uniformly distrubuted fine precipitation with localized regions of coarse blocky particles (6 micron), likely carbides and nitrides. The untested AM IN718 microstructure presented a gamma matrix that contained minimal matrix precipitation, with a localized stringer of carbides and nitrides measuring approximately 1 micron in diameter. The microstructure of the untested monel sample was characterized by equiaxed grains of nickel-copper solid solution with twin boundaries present.

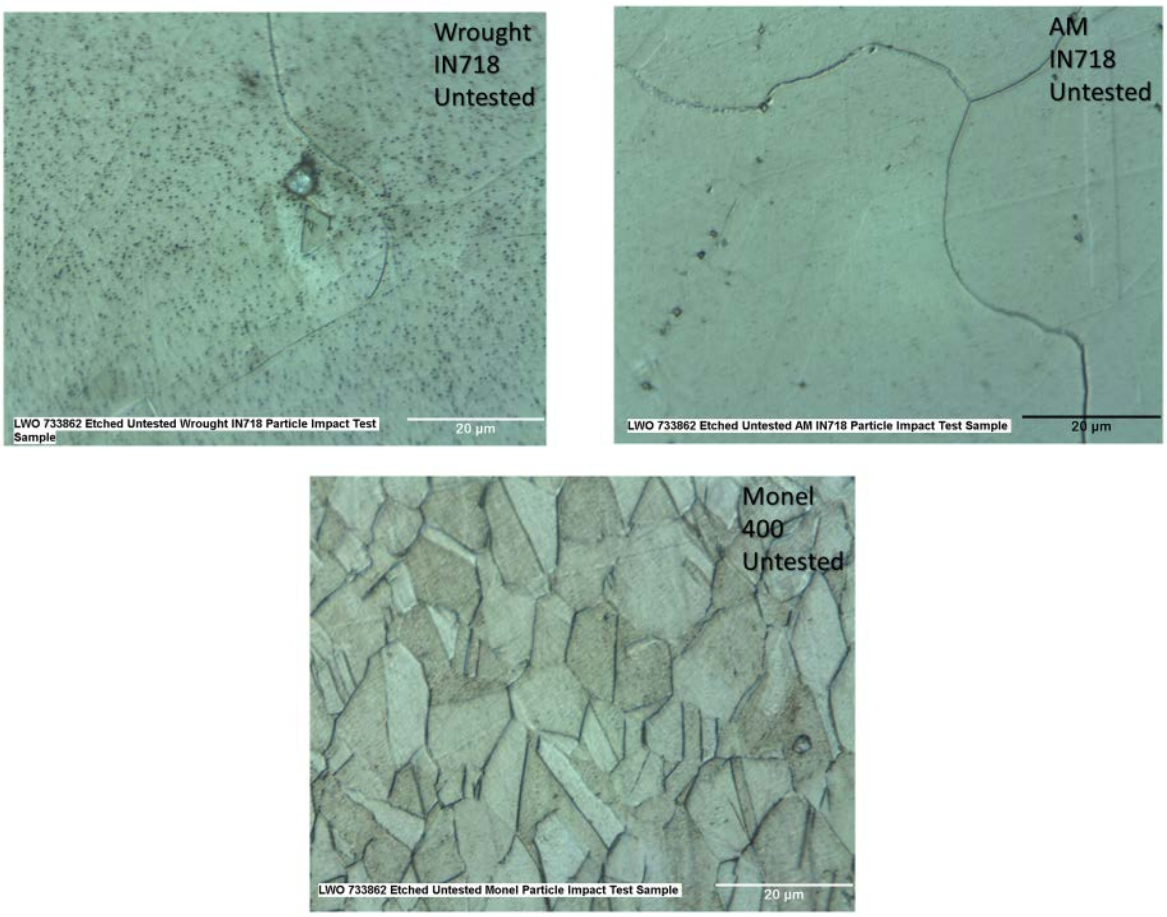

FIG. 17 – Microstructure of untested particle impact test targets: (a) Wrought IN718; (b) AM-IN718; (c) Monel 400.

The microstructure adjacent to the impact craters of wrought IN718 contained coarse, elongated grains at Craters A, B and C, with Crater B exhibiting the greatest deformation and Crater A exhibiting the least. Shear bands were observed within the grains along with needle-like particles and coarse, blocky particles, likely to be delta-phase and carbides, respectively. In contrast, the microstructure at impact overlap consisted of coarse, relatively equiaxed grains also presenting shear bands and delta phase, as well as increasingly coarsened carbides that measured up to 25 microns. The microstructure moving away from the impact crater edge transitioned into equiaxed grains with decreased grain size. At a depth of approximately 0.25 mm, an irreglarly shaped particle was observed, its shape and color typical of an oxide. The microstructure at the impact crater wall of AM-IN718 contained localized regions of elongated grains containing shear bands and segregated regions of carbide precipitation.

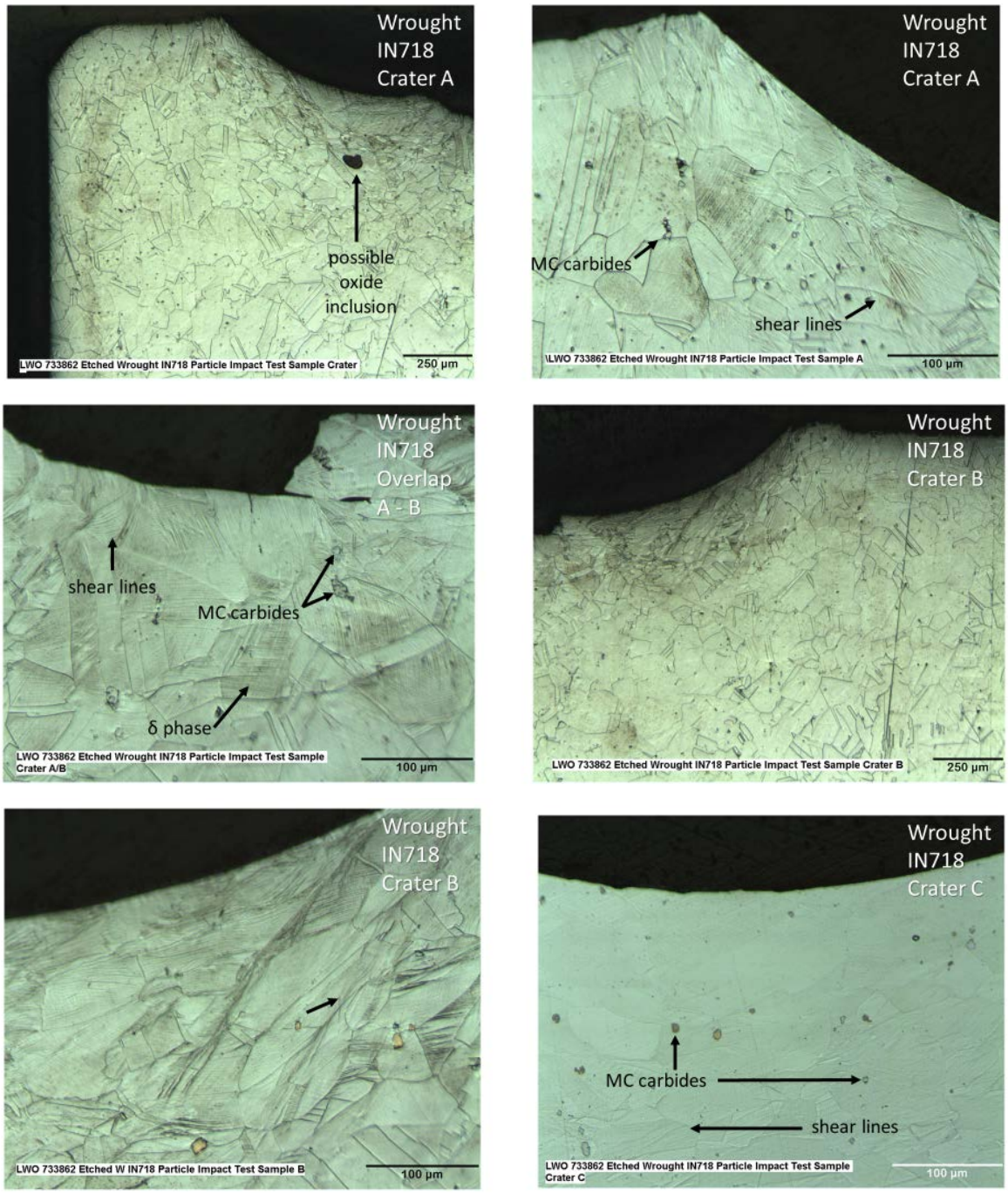

FIG. 18 – Wrought IN718 particle impact test target microstructure adjacent to (a)-(b) Crater A, (c)-(d) Crater B (c) Crater A-Crater B overlap (d) Crater C.

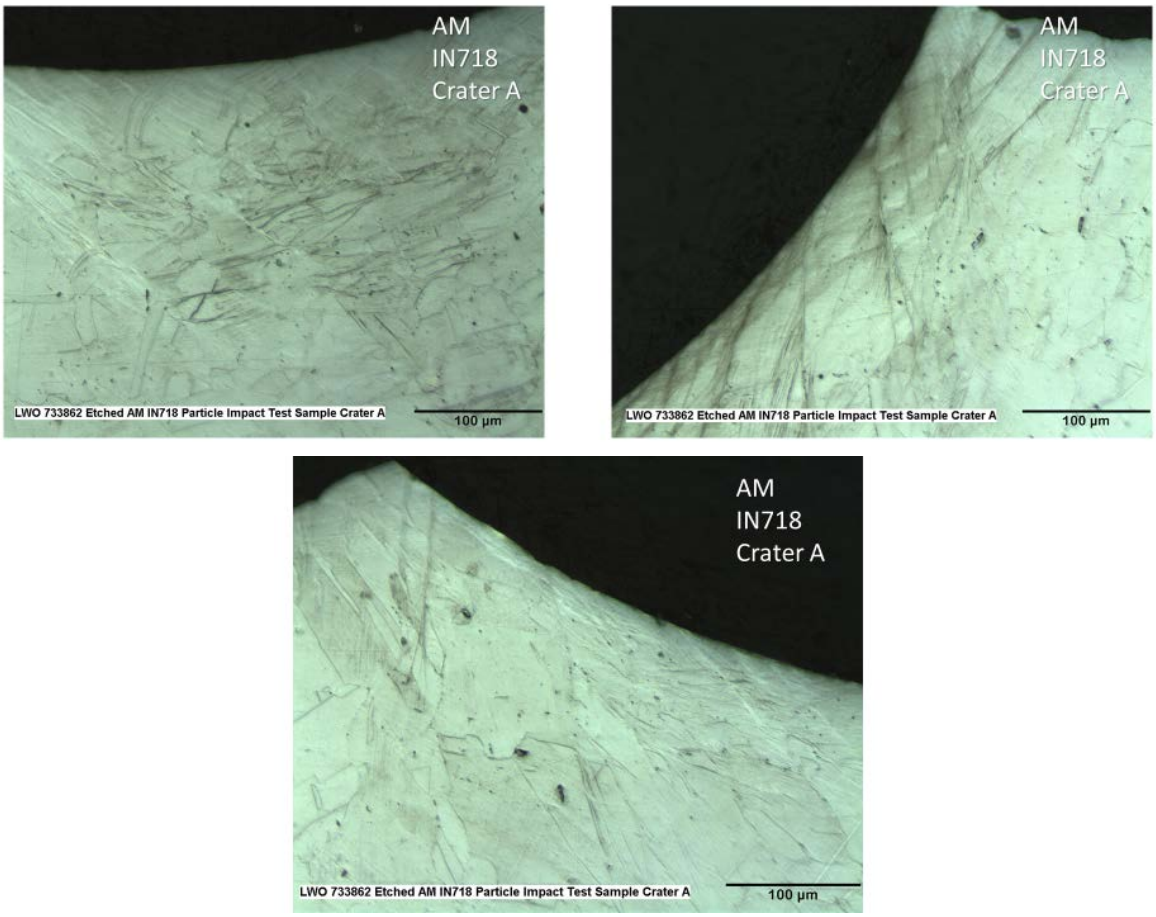

FIG. 19 – AM-IN718 particle impact test target microstructure adjacent to (a) Crater A floor, (c)-(d) Crater A walls.

For the Monel sample, an elongated grain structure was observed along the surface edge adjacent to the crater interface except for at the crater floor, where a more equiaxed grain structure was apparent. A microstructural gradient was present along the crater edge. At the crater floor, a microstructure of slightly elongated grains transformed into a more equiaxed, fragmented grain structure. Moving away from the crater floor, evidence of deformation increased as well-defined, elongated grains were more apparent.

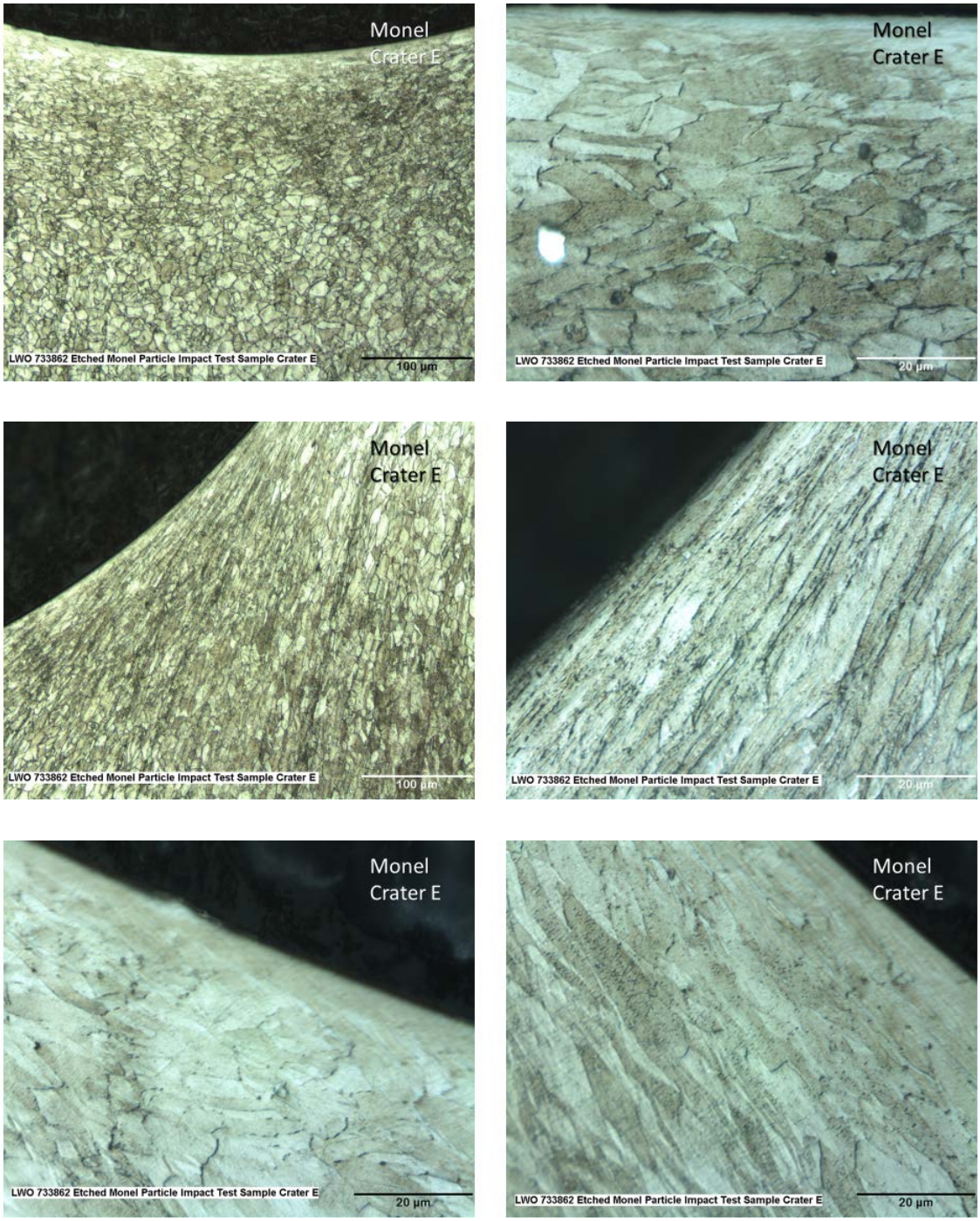

FIG. 20 – Monel 400 particle impact test target microstructure adjacent to (a)-(b) Crater E floor, (c)-(f) Crater E walls.

3.5 Velocity approximation

The single wall penetration equation developed by Burton Cour-Palais is as follows (assuming particle impact occurred normal to the target surface):

$$P = 5.24 d^{19/18} BHN^{-.25} \left(\frac{\rho_p}{\rho_t}\right)^{0.5} \left(\frac{v_0}{c_t}\right)^{2/3}$$

where P is impact crater penetration, d is diameter of the particle, BHN is the Brinell hardness number, ρ_p, ρ_t is density of particle and target material, respectively, v_0 is velocity, and c_t is the speed of sound through the target materials given by

$$c_t = \sqrt{\frac{\left[\frac{E_t}{3(1-2\nu_t)}\right]}{\rho_t}}$$

$$K = \frac{E_t}{3(1-2\nu_t)}$$

where E_t, ν_t and K are Young's modulus, Poisson's ratio, and bulk modulus, repectively, for the target materials.

Velocity upon impact was approximated to be Mach 1.1, Mach 1.3 and Mach 2.2 for wrought, IN718, AM IN718 and Monel 400 test targets, respectively.

Table 2 – Mechanical Properties for Target Materials, Impact Crater Penetration and Projectile Diameter

Sample	E (GPa)	ν_p ($\varepsilon_t/\varepsilon_a$)	K (GPa)	c_t (km/s)	P (cm)	d (cm)	BHN	ρ_p (g/cm^3)	ρ_t (g/cm^3)
W IN718	172	0.272	125.73	3.91813	0.027	0.15	381	3.98	8.19
AM IN718	172	0.272	125.73	3.91813	0.029	0.15	381	3.98	8.19
Monel	180	0.32	166.67	4.32499	0.045	0.15	172	3.98	8.91

Table 3 – Burton Cour-Palais Velocity Approximation

Sample	V (m/s)	(ft/s)	Mach Number
W IN718	393.59	1291.3	**1.15**
AM IN718	449.93	1476.1	**1.31**
Monel	744.8	2443.6	**2.17**

4.0 DISCUSSION

The equiaxed grains observed adjacent to the crater floor may be representative of dynamic recrystalization occuring upon impact of all three samples. The highest energy region is assumed to be at the crater floor, evidenced by the more equiaxed grain structure seen adjacent to this region. The microstructure of coarsened, equiaxed grains adjacent to crater overlap on W IN718 is typical of grain growth achieved by extended annealing. The presence of elongated grains along the crater walls of Monel and W IN718 Crater B suggests cold-working, deformation occuring below the recrystallization temperature, ~$0.5T_m$.

Precipitation also provided insight into heating experienced by the samples upon impact, as increased precipitation was apparent within regions nearest to the crater interface for all three samples. Carbide coarsening and agglomeration is yielded as a result of ageing, thus the crater overlap on W IN718 was determined to be the region to have experienced elevated temperatures for a longer period of time compared to impact Craters A, B and C.

5.0 FUTURE WORK

X-ray microanalysis is recommended to confirm presence of oxide and identify elemental precipitation within microstructure near crater.